Advancing Dynamic Polymer Mechanochemistry through Molecular Gears

Nnamdi M. Ofodum,[†#] Qingkai Qi,[†#] Richard Chandradat,[†] Theodore Warfle,[‡] Xiaocun Lu*[†]

[†]Department of Chemistry & Biomolecular Science, [‡]Department of Chemical & Biomolecular Engineering, Clarkson University, 8 Clarkson Ave, Potsdam, New York 13699, United States.

[#] These authors contribute equally.

ABSTRACT

Harnessing mechanical force to modulate material properties and enhance biomechanical functions is essential for advancing smart materials and bioengineering. Polymer mechanochemistry provides an emerging toolkit to unlock unconventional chemical transformations and modulate molecular structures *via* mechanical force. One of the key challenges is developing innovative force-sensing mechanisms for precise, *in situ* force detection and quantification. This study addresses this challenge by introducing *m*DPAC, a mechanosensitive molecular gear with dynamic and sensitive mechanochromic properties. Its unique mechanoresponsive mechanism is based on the simultaneous configurational variation of its phenazine and phenyl moieties, facilitated by a worm-gear structure. We affirm *m*DPAC's complex mechanochemical response and elucidate its mechanotransduction mechanism through our experimental emission data and comprehensive DFT and MD simulations. The compatibility of *m*DPAC with hydrogels is particularly notable, highlighting its potential for applications in aqueous biological environments as a dynamic molecular force sensor and mapping tool. Moreover, *m*DPAC's multicolored mechanochromic responses enable direct force sensing, visual detection, and real-time quantification, paving the way for integrating molecular gears into bulk materials for precise and real-time mechanical force sensing.

1. INTRODUCTION

Molecular gears, inspired by the intricate molecular machines in biological processes, represent a significant milestone in synthetic and supramolecular chemistry.[1] Their unique structural design enables precise motion control at the molecular level by modulating one part of a molecule to affect another.[2] These gears precisely modulate molecular rotation and torque like nanomachines, similar to macroscopic mechanical systems such as spur[3] and bevel[4] gears. Conventional stimuli like thermal,[5] photo radiation,[6] electronic current,[7] and chemical reaction[8] have been extensively studied for controlling molecular gears. The role of mechanical force—a critical factor in regulating material properties[9] and mechanotransduction in biological systems[10]—has yet to be thoroughly explored as a regulatory mechanism. Current research on molecular gears is primarily limited to solution[11] and surface[12], with a lack of application in bulk materials.

To address these gaps, this study demonstrates how mechanical force precisely modulates molecular configurations and chromism through molecular gearing in bulk hydrogel materials, opening new avenues for dynamically tuning molecular properties.

Vibration-induced emission (VIE)[13] is a typical photoresponsive molecular switch,[14] and its dynamic fluorescence stems from changes in molecular configuration.[15] A prominent example in this category is *N*,*N'*-diphenyl-dihydrodibenzo[a,c]phenazine[16] (DPAC, Figure 1A). In its ground state, the bending and bay angles[16c] ($\theta_{bending}$ and θ_{bay} in Figure 1A) are crucial for accessing the curvature of the phenazine moiety (the blue part of DPAC in Figure 1A) and the orientation of the phenyl rings (the grey part of DPAC in Figure 1A), respectively. The fluorescence of DPAC is closely linked to its structural transformations upon photoexcitation.[15] Specifically, when activated by a certain wavelength (typically 350-380 nm),[13a] the phenazine moiety transitions from a bent to a planar state (Figure 1B). Such a change causes the two attached phenyl rings to reorient perpendicularly to the phenazine moiety, leading to a concurrent increase in both bending and bay angles (Figure 1B). Turning off UV radiation reverts the phenazine moiety from a planar back to the bent configuration. Although DPAC is not conventionally classified as a molecular gear,[2a] the coordinated configurational changes in its various moieties indicate a strong potential for mechanical modulation of its structure, which can significantly influence DPAC's fluorescent properties.

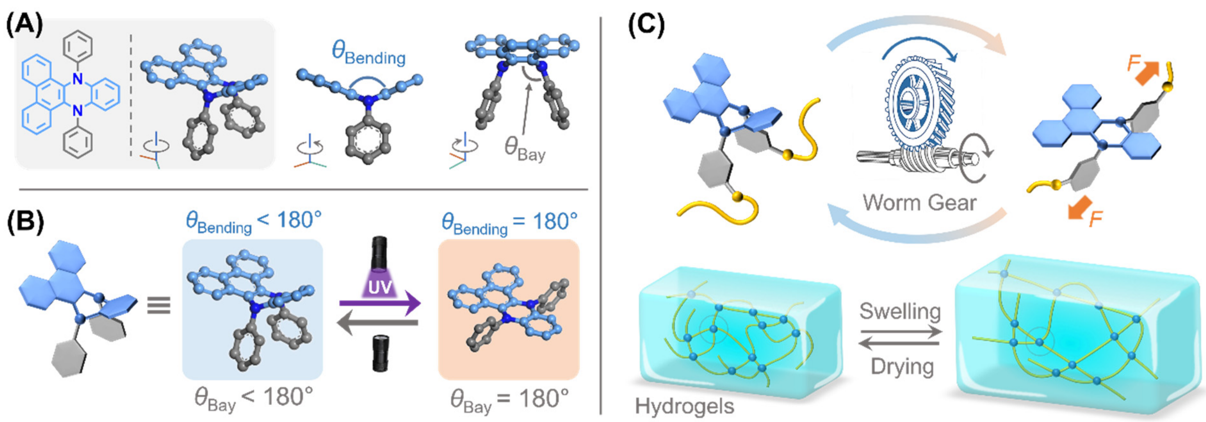

Figure 1. (A) DPAC structure with definitions of bending and bay angles. **(B)** Reversible photoactivation of DPAC, illustrating changes in bending and bay angles during the activation and deactivation processes. **(C)** Design strategy of DPAC molecular gears and its mechanochromism validation through hydrogel swelling and drying.

Utilizing mechanical force to tune molecular structures and modulate chemical transformations has become a focus area in polymer mechanochemistry over the last decade.[9a, 17] This approach has emerged as a vital tool for uncovering unconventional reaction pathways,[18] developing mechanoresponsive materials,[19] and advancing biomedical diagnostics and therapeutics.[20] Polymer mechanochemistry excels in revealing molecular-level force information by employing mechanophores, which are molecular and nanoscale structural units undergoing structural variations or chemical transformations in response to external mechanical forces.[9b, 21] The fundamental design principle involves embedding mechanophores strategically into polymer chains and incorporating them into polymer matrices. External mechanical forces are transduced through the polymer chains from the macroscale level, cascading across multiple scales to activate the mechanophores, thereby triggering their mechanochemical responses. Classical mechanophores, such as spiropyran,[22] naphthopyran,[23] and tetraarylsuccinonitriles (TASN),[24] display color changes *via* chemical transformations when mechanically activated. Another type of mechanochromism involves mechanically induced configurational changes, as seen in mechanophores like flapping molecular force probes (FLAP),[25] fluorescent flippers,[20a] conformer ring flip,[26] diarylethene,[27]and azobenzene[28]. However, mechanically controlled molecular gears have yet to be extensively explored and understood. A comprehensive understanding of mechanoresponsive molecular gears could significantly broaden the scope of polymer mechanochemistry and introduce a novel class of mechanophore for precision force control and dynamic mechanochemical responses.

When exploring the approach to mechanically control DPAC, we employed several design strategies to precisely manipulate the configurational change in DPAC's phenazine moiety, aiming to dynamically tune its fluorescent properties by mechanical force. A direct method was to apply mechanical force to stretch both ends of the phenazine moiety in DPAC, thereby influencing its bending angle. An increased stretch led to a larger bending angle. However, this approach posed significant synthetic challenges, primarily due to the obstacles in functionalizing the phenazine unit with appropriate groups for force application. Alternatively, we have investigated a molecular gearing pathway for transducing mechanical force. We noted that the bending and bay angles increased and decreased simultaneously during photoactivation and subsequent deactivation.[29] This observation raised an intriguing question about the interplay and correlation between these angles. We hypothesize that a mechanically tuned bay angle could induce corresponding changes in the bending angle *via* molecular gearing. This mechanism, where the bay and bending angles are perpendicular to each other, resembles the function of a worm gear, providing indirect, non-coplanar control of molecular motions (Figure 1C). In this study, we successfully integrated DPAC into hydrogels, utilizing hydrogel swelling and drying[25, 30] to validate DPAC's dynamic mechanochromism *via* molecular gearing. This work highlights the potential of DPAC-based molecular gear in biological applications and underscores its precision and dynamic mechanochemical response.

2. RESULTS AND DISCUSSION

2.1. DFT-based CoGEF simulation

CoGEF simulation. We first utilized a density functional theory (DFT)-based simulation method, constrained geometries simulate external force (CoGEF),[31] to access the potential mechanochemical response of DPAC. The CoGEF method simulates the impact of mechanical force on molecular configurations and bonding by designating two terminal groups as constrained pulling points and incrementally extending the distance between them.[32] This procedure, which undergoes geometry optimization under constraint at each step, effectively replicates molecular extension and enables the prediction of structural and bonding changes due to molecular stretching throughout its reaction trajectory. Our exploration of molecular-gear-facilitated force transduction in DPAC involved applying mechanical force to the attached phenyl rings (Figure 2A, grey rings) to manipulate the bay angle. We aimed to gradually increase the distance between the two pulling groups (Figure 2A, methyl groups in yellow) and examine how alterations in the bay angle affect the bending angle. The rationale behind selecting these specific pulling points will be discussed later. For now, we use the pulling groups at the *meta* position, termed *m*DPAC (Figure 2A), to demonstrate the mechanochemical activity of DPAC. As shown in Figure 2A, the stepwise stretching led to a gradual increase in the bay angle from 106° to 148° and a corresponding rise in the bending angle from 136° to nearly 180° (Figure 2D). The stretch ratio on the upper horizontal axis represents the ratio of the pulling distance to the equilibrium distance prior to stretching. The molecular energy profile also increased in conjunction with the stretching distance (Figure 2E). Initially, we observed an almost linear rise in energy, requiring a maximum force of about 0.5 nN, until the bending angle reached 160°. Beyond this angle, a substantial increase in energy was observed, with the maximum force required escalating to 2.5 nN.

Planarity analysis of the phenazine moiety. We assessed the planarity of the phenazine ring during the stretching process in subsequent analyses. The bending angle shown in Figure 2D was calculated based solely on the central piperazine configuration, which may not fully capture the overall planarity of the phenazine moiety. Therefore, we introduced two additional parameters: molecular planarity parameter (MPP) and span of deviation from plane (SDP).[33] MPP calculates the root-mean-square deviation of the atoms from the best-fit plane, while SDP measures the range of deviation within the system relative to this plane (Figure 2B).[33] Both parameters provide a quantitative assessment of planarity, with lower values indicating better planarity. The MPP and SDP of the phenazine moiety were calculated using the Multiwfn software.[34] Our results, as depicted in Figure 2F, show a decrease in both MPP (from 0.55 to 0.2 Å) and SDP (from 0.95 to 0.6 Å), suggesting enhanced planarity of the phenazine ring upon stretching. Furthermore, the conjugation length of the phenazine moiety was extended as the bending angle increased.

To examine the π electronic structure of the phenazine moiety during stretching, we utilized the localized orbital locator (LOL),[35] specifically LOL-π,[36] to explore the π electron delocalization status. The isosurface[37] of LOL-π for the phenazine moiety, with an isovalue set at 0.15, was visualized in Figure 2C. The unstretched DPAC displayed a discrete conjugation state (Figure 2C, structure 1) without constraints. However, as the bending angle increased, the nitrogen atoms in the central piperazine began to participate in the conjugation, effectively bridging the previously discrete conjugation sections (Figure 2C, structures 2 and 3).

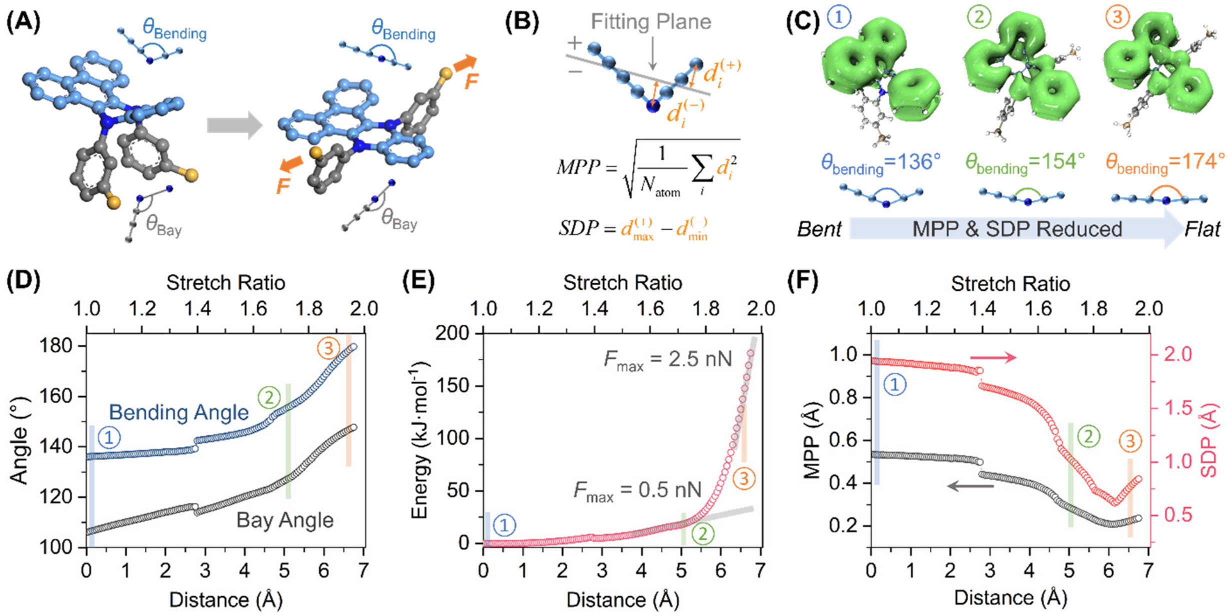

Figure 2. (A) Demonstration of mechanical stretching for *m*DPAC using CoGEF simulation and illustration of stretch-induced changes in bending and bay angles. **(B)** Definition of MPP and SDP[33] for planarity evaluation of the phenazine moiety. **(C)** LOL-π isosurface[37] for the phenazine moiety with an isovalue of 0.15. Three representative *m*DPAC configurations during stretching where MPP and SDP decreased as bending angles increased. The visualization was generated using the Multiwfn software[34] and rendered by the VMD program[38]. **(D)** Coordinated increase in bending and bay angles with increasing the distance between the two pulling points as denoted in (A), as simulated by CoGEF. **(E)** Energy profile of *m*DPAC during stretching, highlighting two distinct phases of maximum required force. **(F)** Decrease in MPP and SDP with increased pulling distance, indicating enhanced planarity of the phenazine moiety. The calculations of MPP and SDP were conducted using the Multiwfn software.[34] The CoGEF simulations were conducted with PBE0/6-31G* level of theory[39] with the EFPCM[40] solvation model using the Gaussian 16 software package.

The CoGEF simulation reveals that mechanically induced changes in the bay angles lead to a simultaneous increase in DPAC's bending angle, confirming the molecular gearing motion of DPAC in response to mechanical force. Furthermore, the low-energy transition from discrete to continuous conjugation states in the phenazine unit highlights DPAC as a promising mechanophore candidate for dynamic mechanochromic applications.

2.2. Synthesis and hydrogel formation

The synthetic work involved the synthesis of *m*DPAC mechanophore and its incorporation into polymer matrices for mechanochemical demonstration (Scheme 1). Based on *m*DPAC's mechanosensitivity predicted by the CoGEF simulation, we employed hydrogel swelling and drying to generate a controllable and reversible external force for *m*DPAC. The synthesis began with commercially available phenanthrenequinone, which reacted with 3-bromoaniline to form an imine derivative, followed by a reduction by $NaBH_4$ to form the amine-based precursor **1**. A subsequent cyclization reaction between **1** and difluorobenzene yielded precursor **2**. The bromo groups in **2** underwent further transformations, including formylation, reduction, and acylation, to produce an *m*DPAC crosslinker **5** with two terminal methacrylate groups that acted as crosslinking agents within the hydrogel. The *m*DPAC-functionalized hydrogel was then synthesized through the photopolymerization of 2-hydroxyethyl acrylate (HEA), using a crosslinker mixture of ethylene glycol dimethacrylate (EGDMA) and the *m*DPAC crosslinker **5** in a 9:1 molar ratio. The hydrogel was extensively washed to remove unreacted substances, followed by vacuum drying to yield a dry and transparent film.

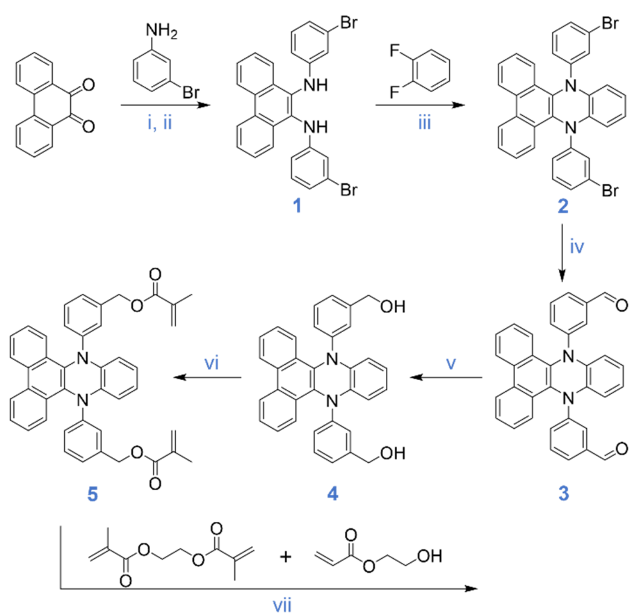

Scheme 1. Synthetic route of *m*DPAC mechanophore and hydrogel formation: (**i**) $TiCl_4$, toluene, 20 °C, 12 h; (**ii**) $NaBH_4$, ethanol, 20 °C, 6 h; (**iii**) NaH, dry DMF, 120 °C, 12 h; (**iv**) *n*BuLi, dry DMF, dry THF, -78 °C, 2 h; (**v**) $NaBH_4$, ethanol, 20 °C, 12 h; (**vi**) DMAP, methacrylic anhydride, dry THF, 20 °C, 12 h; (**vii**) bisacylphosphine oxides (BAPOs), white light, 20 °C, 2 h.

2.3. Mechanical activation of *m*DPAC *via* hydrogel swelling

Optimization for hydrogel swelling. We first optimized the conditions for hydrogel swelling and drying for mechanochemical testing. As hydrogels swell, their internal volume increases, stretching the polymer network and thereby exerting force on the polymer backbone. The degree of stretching and the consequent force is directly proportional to the swelling volume: larger volumes result in greater stretching distances and more substantial forces. *m*DPAC served as a crosslinker in the hydrogel matrix. During the swelling phase, the crosslinked *m*DPAC was stretched in response to the hydrogel's expanding volume, while the drying process reverted them to their unstretched states. To fine-tune hydrogel properties, we screened with various crosslinking densities ranging from 0.1% to 1%. We observed that lower crosslinking densities led to higher swelling ratios and quicker swelling rates (Figure S22). However, low density was also correlated with diminished mechanical strength post-swelling. Therefore, we determined an optimal crosslinking density of 0.3%, balancing swelling efficiency, kinetics, and sample integrity.

We employed a range of solvents for swelling tests: water, acetone, DMF, acetonitrile, DMSO, and methanol (Figure S24). Each solvent consistently reached a steady emissive state within 40 minutes, which we established as a standard duration for all our swelling tests (Figure 3C and S22). Among all the tested solvents, acetonitrile, acetone, and methanol showed relatively minor swelling ratios, with less than a two-fold increase in volume (Figure S24). Water showed an intermediate swelling ratio, doubling the hydrogel volume upon complete swelling (Figure 3A). In contrast, DMF and DMSO induced the most significant swelling ratios, with volumes increasing to more than four times their original size (Figure 3A and S23). Due to the drying challenges associated with DMSO, which affected the subsequent reversibility tests, we selected DMF for a large swelling ratio and water for an intermediate swelling ratio.

Mechanical activation of *m*DPAC through hydrogel swelling. As both ends of *m*DPAC were connected to the polymer backbones, the displacement applied to *m*DPAC during hydrogel swelling was estimated based on the increased swelling ratio. As depicted in Figure 3B, the stretch ratios applied to *m*DPAC with water and DMF were determined to be 1.5 and 2.0, respectively, aligning with the CoGEF simulation results shown in Figure 2. Under an excitation wavelength of 365 nm, the dry hydrogel exhibited a strong blue emission at 436 nm, validating the bent configuration of DPAC (Figure 3D). Upon swelling with water and DMF, the hydrogels exhibited emissions in cyan and green, peaking at 505 nm and 556 nm, respectively (Figure 3D and 3E). The observed differences between water and DMF swelling implied that larger displacement distances resulted in a flatter bending angle in *m*DPAC, leading to a red shift in the emission wavelength. The experimental results aligned with CoGEF simulations in Figure 2. When the hydrogel was dried, its volume returned to its original size, and concurrently, the *m*DPAC fluorescence shifted back to its dry state (Figure S28), indicating a reversible transition to the bent configuration. The reversible activation and deactivation of *m*DPAC were consistently observed across multiple swelling/drying cycles (Figure 3F), with each cycle maintaining stable and consistent peak wavelengths.

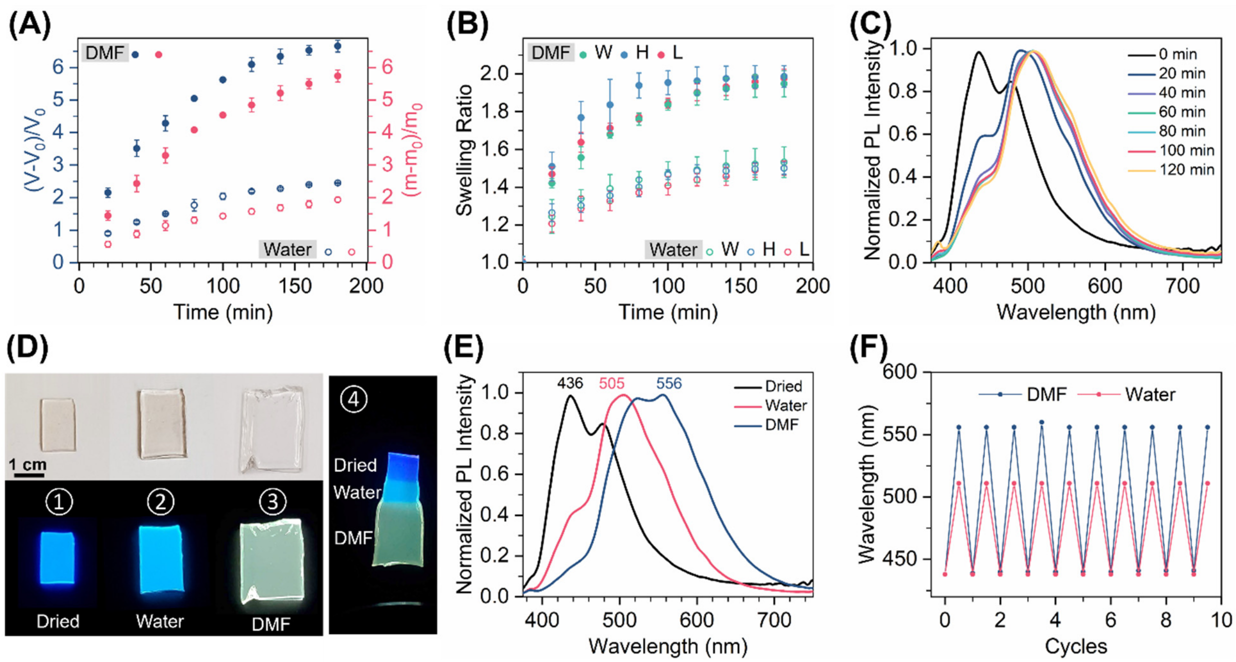

Figure 3. (A) Swelling volume and mass ratios of *m*DPAC hydrogels for water and DMF. **(B)** Dimensional changes in hydrogels swollen by water and DMF, including width (W), height (H), and length (L). **(C)** Swelling rate and kinetics in water, monitored by fluorescence spectra under an excitation wavelength of 365 nm. **(D)** *m*DPAC hydrogel samples in dried (sample 1) and swollen states with water (sample 2) and DMF (sample 3) under white light (top) and UV light (bottom). Sample 4 illustrated the influence of swelling ratio on fluorescence within a single sample. This sample was sequentially swollen by water and then DMF using the same specimen. The scale bar represents 1 cm. **(E)** Fluorescence spectra of *m*DPAC hydrogels between dried and swollen states with water and DMF under an excitation wavelength of 365 nm. **(F)** Shifts in emissive peak wavelength through multiple swelling-drying cycles with water and DMF.

2.4. MD simulation and *m*DPAC conformers

Configurational isomers of *m*DPAC. We implemented molecular dynamics (MD) and DFT simulations to further elucidate *m*DPAC's mechanical activation mechanism. Initially, MD simulations using GFN1-xTB[41] were conducted to explore *m*DPAC's potential configurations. We captured molecular trajectories over 1000 ps, recorded structures every 50 fs, and used root-mean-square deviation (RMSD) analysis to track configuration changes. RMSD,[42] a widely used metric for comparing atomic coordinates, indicates that lower values signify closer structural similarity. Figure 4B illustrates RMSD variations of *m*DPAC structures compared to their initial configuration, revealing three primary low-energy configurational isomers, *m*DPAC-1, 2, and 3 (Figure 4A). These conformers were identified based on the MD-simulated configurations with the lowest energies sorted by the Molclus[43] software. These conformers all maintained a bent phenazine moiety and only differed in the orientation of their substituent methyl groups (Figure 4A, yellow balls) attached to the phenyl rings (Figure 4A, grey rings). *m*DPAC-1 and *m*DPAC-2 featured the substituted methyl groups aligning in the same direction, while *m*DPAC-3's substituents pointed in opposite directions. Continuous interconversion among these *m*DPAC conformers was observed throughout the simulations, irrespective of the conformer initially used as the starting configuration. (Figure S20-20). Subsequently, these *m*DPAC conformers were subject to DFT simulations to compare their energies using the M06-2X-D3(zero)/TZVP[44] level of theory in both vacuum and solvated states. The energy comparison, summarized in Figure 4C, demonstrated a significant reduction in *m*DPAC energy due to solvation. In solvents like water and DMF, *m*DPAC-1 showed the lowest energy, with only a minor energy difference of approximately 2 kJ·mol^{-1} among the conformers. These small energy barriers elucidate the constant interconversion observed during the MD simulations (Figure 4B, S19-20).

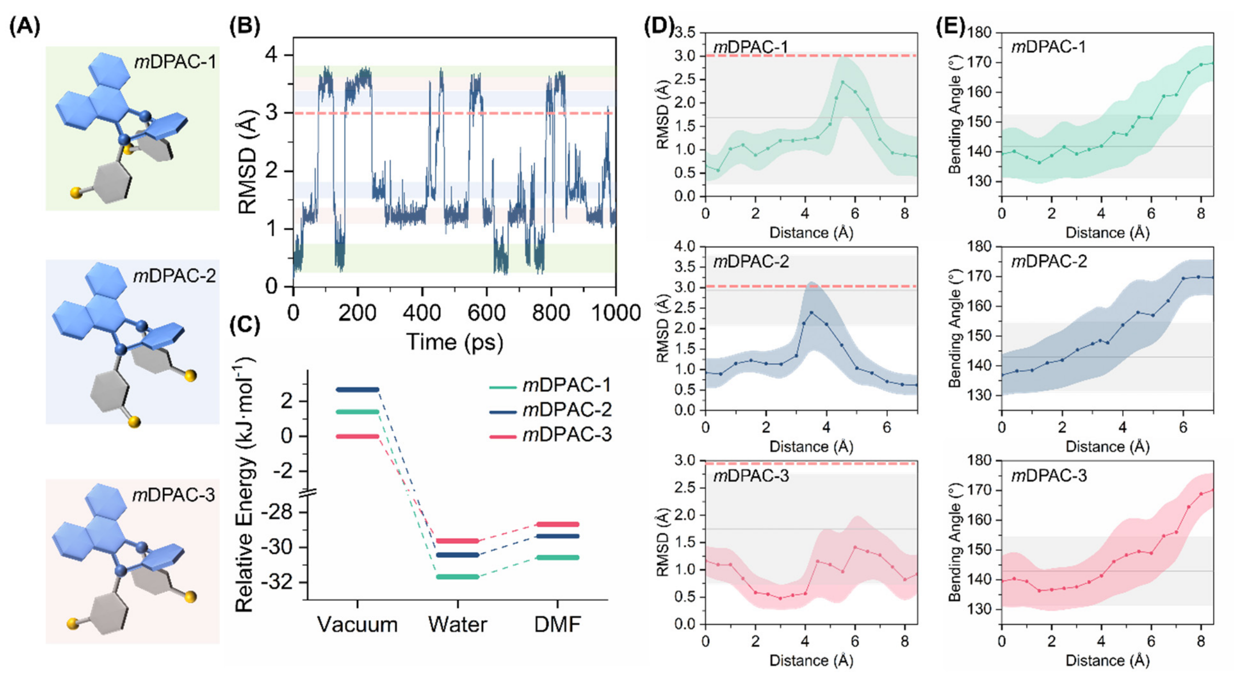

Figure 4. (A) Identification of three primary *m*DPAC conformers based on RMSD analysis from the MD trajectory. These conformers were identified based on the MD-simulated configurations with the lowest

energies sorted by the Molclus[43] software. **(B)** MD simulation of unconstrained *m*DPAC with *m*DPAC-1 as the initial structure, using GFN1-xTB[41] to capture the molecular trajectory over 1000 ps at 600K, recording structures every 50 fs. RMSD for each frame was retrieved using the VMD program.[38] The red dashed line at 3 Å indicates the flipping threshold for the phenazine moiety of *m*DPAC conformers, with colored shades representing RMSD for *m*DPAC-1, 2, and 3, the same color shades as in (A). **(C)** Energy comparison between *m*DPAC conformers in vacuum and solvated (water and DMF) states, calculated in Gaussian 16 using the M06-2X-D3(zero)/def-TZVP level of theory[44] with the EFPCM[40] solvation model. **(D)** RMSD range is narrower under constraints (colored shade) than unconstrained (grey shade) states, which captured the molecular trajectories over 200 ps at 600K with constraint terminal groups using GFN1-xTB. RMSD for each frame retrieved by the VMD program,[38] with the red dashed line indicating the 3 Å flipping threshold, as shown in (B). The shades represent the standard deviation of RMSD under constrained (colored) and unconstrained (grey) conditions. **(E)** Increased bending angles of all three *m*DPAC conformers with elongated constraint distance, with the standard deviation of bending angles under constrained (colored) and unconstrained (grey) conditions, respectively.

***m*DPAC conformers under force constraints**. We further examined the impact of force constraints on the DPAC conformers, employing a methodology similar to our previous CoGEF simulations (Figure 2). We conducted MD simulations under constrained conditions, maintaining a fixed distance between the terminal pulling groups (Figure 4A, yellow balls) at the *meta*-position of the phenyl rings. Altering the constraint distance revealed significant variances in molecular motion compared to the unconstrained configurations (Figure S16-18). The correlation between the constraint distance and the average RMSD for each *m*DPAC conformer was presented in Figure 4D, illustrating the influence of force constraints on molecular configurations. The colored shade in each plot represents the standard deviation of the averaged RMSD. Unconstrained *m*DPAC displayed a broader RMSD range (Figure 4D, grey shade) than its constrained counterparts, indicating limited motion and reduced configurational variation under mechanical force. Notably, these constraints also inhibited the flipping of the phenazine moiety, a phenomenon observed in the unconstrained *m*DPAC (Figure 4B). In Figure 4B, a red dashed line at RMSD = 3 Å indicated the flipping threshold; beyond this value, the phenazine moiety transitioned to a mirror-image configuration. The RMSD values of constrained *m*DPAC isomers consistently remained below the 3 Å flipping threshold, suggesting no inversion of *m*DPAC's phenazine moiety and restricted molecular flexibility (Figure 4D).

Furthermore, we evaluated the bending angle of the phenazine moiety in each frame of the MD simulation. As depicted in Figure 4E, the bending angle increased proportionately to the constraint distance, culminating in an almost flat configuration of the phenazine moiety at larger displacements. Overall, the

MD simulations revealed that all three primary *m*DPAC conformers exhibited restricted motion under applied force. Applying these force constraints prevented the flipping of the phenazine and led to a progressive increase in the bending angle, approaching a nearly flat configuration with larger constraint displacements. These results validate the hypothesis that *m*DPAC undergoes molecular gearing motion, with the bending and bay angles changing continuously and concurrently in response to varying mechanical forces.

2.5. Absorption and emission of *m*DPAC

Emission simulation of *m*DPAC conformers. To further elucidate and validate the mechanically activated fluorescence of *m*DPAC, we utilized time-dependent density functional theory (TD-DFT)[45] simulations. Initially, CoGEF was performed on the ground state (S0) using the PBE0/6-31G* level of theory. The CoGEF results for all three *m*DPAC conformers were represented by the blue curves in Figure 5A-C. Under small stretch ratios, the phenazine moiety maintained a bent configuration with the two attached phenyl rings aligning either symmetrically (Figure 5D, green shade) or asymmetrically (Figure 5D, blue shade). As the constraint distance between terminal groups increased, the bending angle enlarged, leading to a flatter phenazine moiety, as evidenced by a reduced MPP and SDP (Figure S6-11). The phenazine moiety also adopted a twisted configuration (Figure 5D, yellow shade), akin to a recently reported photoactivated DPAC derivative,[29] in which the two attached phenyl rings were oriented perpendicularly. Such configuration was only observed in *m*DPAC-1 and *m*DPAC-3 at a large stretch ratio in the S0 state. These optimized structures in the S0 state were used to predict absorption wavelengths.

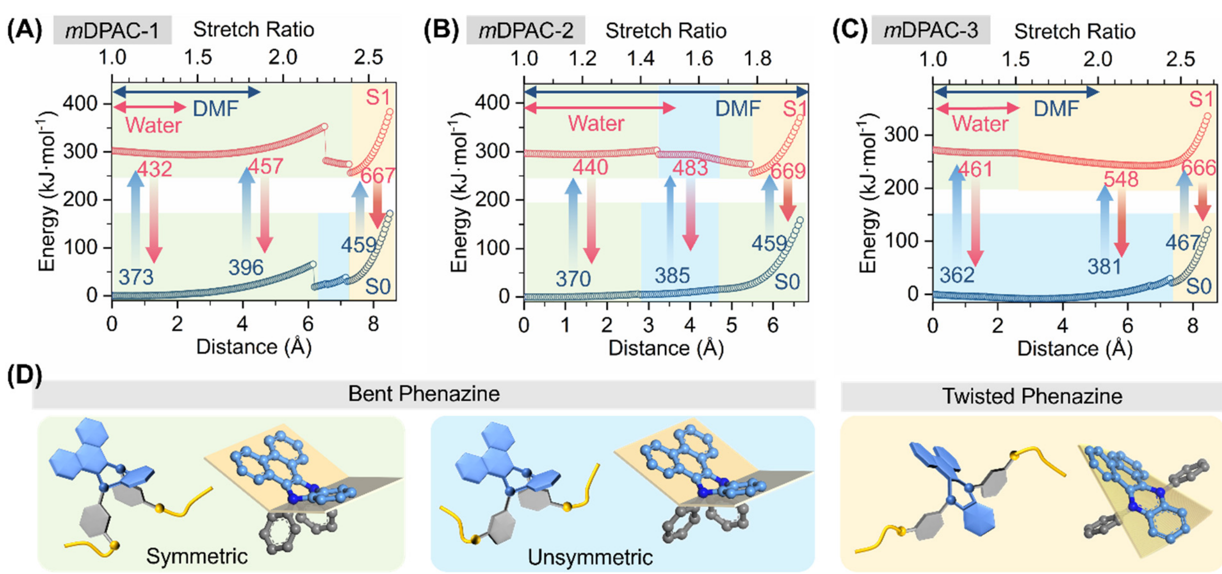

Figure 5. CoGEF simulation results for ground state (S0, blue curves) and excited state (S1, red curves) of the three primary *m*DPAC conformers: **(A)** *m*DPAC-1, **(B)** *m*DPAC-2, and **(C)** *m*DPAC-3. The CoGEF

simulation utilized the PBE0/6-31G* level of theory[39] in Gaussian 16. Blue and red numbers in (A)-(C) indicate representative absorption and emission wavelength in different stages of stretching, respectiely. Wavelengths for absorption and emission were determined from CoGEF-simulated configurations, with energy calculations performed at the M06-2X-D3(zero)/def-TZVP level of theory[44] using the EFPCM[40] solvation model. Arrows next to the axis of stretch ratio in (A)-(C) show the single-dimensional stretch range for water (red) and DMF (blue) based on experimental swelling ratios. **(D)** Three major configurations during the molecular stretching observed from the CoGEF simulation. Twisted phenazine moiety started to emerge with a relatively large stretch ratio. The colored shades in (A)-(C) represented corresponding configurations as illustrated in (D).

Similarly, we conducted CoGEF analysis on the excited state (S1) using the same DFT functional and basis set as the ground state (S0). During stretching, the S1 state revealed significantly different energy states and configurations compared to the S0 state. The energy level in S1 was markedly higher than S0 energies, and the twisted phenazine configuration (Figure 5A-C, yellow shade) emerged in all three *m*DPAC conformers in the S1 state. The twisted phenazine configuration in *m*DPAC-3 began to emerge at a stretch ratio of 1.5, lower than that for *m*DPAC-1 (2.6) and *m*DPAC-2 (1.75), resulting in a more significant red-shift in emission. The optimized configurations in the S1 state at specific constrained distances were used to evaluate the emission wavelengths of *m*DPAC. Figure 5A-C present three representative absorption and emission wavelengths for each *m*DPAC conformer. At a small stretch ratio of 1.5, *m*DPAC-2 and *m*DPAC-3 began to exhibit significant bathochromic shifts upon mechanical activation. Conversely, *m*DPAC-1 required a stretch ratio larger than 2 to show a significant red shift in fluorescence. The working range of water and DMF for each *m*DPAC conformer was labeled in Figure 5A-C based on the single-dimensional swelling ratio of water (1.5) and DMF (2.0), as shown in Figure 3B. During water swelling, only *m*DPAC-2 exhibited significant red-shifted fluorescence. With DMF, a solvent with a larger swelling ratio, both *m*DPAC-2 and *m*DPAC-3 displayed significant red-shift. Meanwhile, *m*DPAC-1, requiring a large stretch ratio for observable red-shifted fluorescence, did not achieve such shifts under water or DMF swelling. The coexistence of the three *m*DPAC conformers with different mechanical stretch sensitivity resulted in experimental emissions covering a wide range of wavelengths and shoulders, suggesting that *m*DPAC has the potential to respond to even larger mechanical stretch ratios.

2.6. Regioselectivity of *m*DPAC

Mechanochemical regioselectivity. Following the successful demonstration of *m*DPAC's mechanochromism, we broadened our investigation to assess DPAC's mechanochemical regioselectivity, particularly focusing on how varying locations of applied force affect the mechanochemical reactivity of DPAC. Attaching polymer chains to non-*meta* positions notably altered DPAC's mechanochromic activity.

In DMF-swollen hydrogels, *para*-substituted DPAC (*p*DPAC, Figure 6A) displayed a blue hue with diminished fluorescent intensity (Figure 6C) and exhibited a less significant red shift to 498 nm compared to *m*DPAC's shift to 556 nm (Figure 6D). CoGEF simulations revealed consistent bent configurations for *p*DPAC in both the ground (S0) and excited (S1) states (Figure 6E), with bending angles varying only from 134° to 142° during stretching (Figure 6F, S12-13). Notably, even with an increased stretching ratio of 2, the bending angle of *p*DPAC showed only a slight increase, resulting in a marginal shift in the peak emission wavelength from 460 nm to 478 nm (Figure 6D), in stark contrast to *m*DPAC's larger red-shift under the same conditions.

The minimal mechanochemical activity observed in *p*DPAC can be attributed to the rotational constraints of its phenyl rings, which hindered the formation of a flat phenazine configuration that is essential for a significant mechanochromic response. As shown in Figure 6B, steric hindrance, notably between the orange-highlighted hydrogens, prevented the phenazine from achieving a flat configuration, which required a perpendicular orientation between the phenyl and phenazine rings. In contrast, for *m*DPAC conformers, mechanical stretching aided in the rotation of the phenyl rings, thus facilitating a flat phenazine configuration. Figure 6F illustrates the bending angle difference between *p*DPAC and *m*DPAC: with increased pulling distance, the bending angle of *p*DPAC's phenazine moiety remained constrained within a narrow range (134-142°), whereas *m*DPAC showed a steadily increasing bending angle during stretching, reaching an almost flat state (greater than 170°).

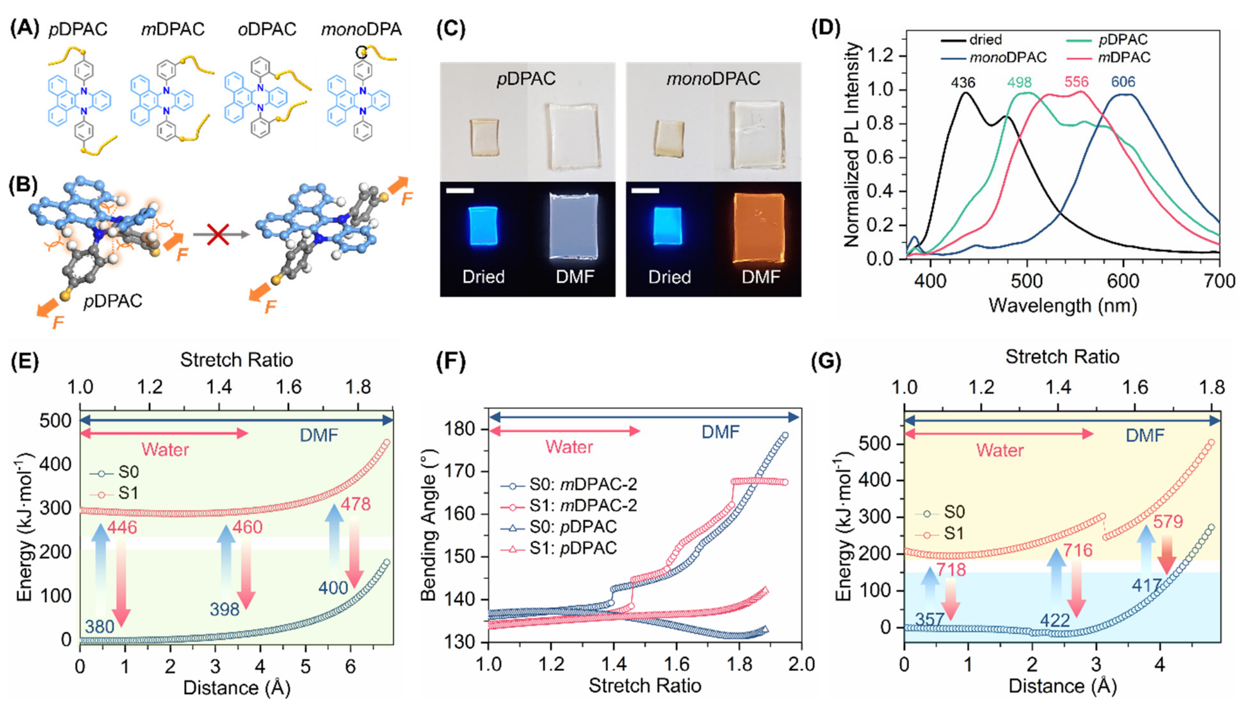

Figure 6. (A) Structures of regioisomers (*p*DPAC, *m*DPAC, *o*DPAC) and control structure (*mono*DPAC). **(B)** Illustration of steric hindrance impeding the mechanochemical response in *p*DPAC. **(C)** *p*DPAC and *mono*DPAC hydrogel samples in dried and swollen states with DMF under white light (top) and UV light (bottom). The scale bar represents 1 cm. **(D)** Fluorescence spectra of hydrogels with DPAC regioisomers and *mono*DPAC between dried and swollen states in DMF under an excitation wavelength of 365 nm. CoGEF simulation results for ground state (S0, blue curves) and excited state (S1, red curves) of **(E)** *p*DPAC and **(G)** *o*DPAC. The CoGEF simulation was conducted at the PBE0/6-31G* level of theory[39] utilizing Gaussian 16. Blue and red numbers in (E) and (G) represent absorption and emission wavelengths at different stretching stages, respectively. Wavelengths for absorption and emission were determined from CoGEF-simulated configurations, with energy calculations performed at the M06-2X-D3(zero)/def-TZVP level of theory[44] using the EFPCM[40] solvation model. Arrows next to the stretch ratio axis in (E) and (G) indicate the uniaxial tensile range for water (red) and DMF (blue) based on experimental swelling ratios. **(F)** Comparison of bending angles between *m*DPAC and *p*DPAC with increasing stretch ratio: *m*DPAC exhibited an increasing bending angle, while *p*DPAC showed no significant change.

Furthermore, *ortho*-substituted DPAC (*o*DPAC, Figure 6A) exhibited distinctly different CoGEF curves for both the ground (S0) and excited (S1) states (Figure 6G). In its ground state (S0), *o*DPAC retained a bent configuration, while in the excited state (S1), it exclusively adopted twisted phenazine configurations, similar to Figure 5D. These configurations resulted in a significant red-shift in emission, exceeding 600 nm. However, due to synthetic challenges, we could not successfully synthesize an *o*DPAC hydrogel. Detailed CoGEF simulation results for *o*DPAC are provided in the supporting information.

2.7. Control hydrogels with *mono*DPAC.

To further confirm the mechanochromism of DPAC, we employed a control hydrogel to validate DPAC's mechanochromic response, specifically ensuring that the swelling-induced chromic changes were due to mechanical input and not other stimuli. The mechanical activation of DPAC relied on applying force at two pulling points on the molecule for effective stretching. If only one end of DPAC is attached to the polymer network, no mechanical force can be efficiently applied to the DPAC unit. Therefore, we synthesized a control structure, *mono*DPAC, with only one phenyl ring attached to the polymer network (Figure 6A). No stretch force was applied to *mono*DPAC during swelling. The DMF-swollen *mono*DPAC hydrogel exhibited distinct orange fluorescence (Figure 6C) peaking at 606 nm (Figure 6D), indicative of the phenazine moiety of *mono*DPAC adopting a fully flat configuration.[29] This fluorescence wavelength from *mono*DPAC in hydrogels closely resembled its emission in solution, suggesting that in the absence of mechanical constraints, DPAC underwent a photo-induced flat configuration, similar to its photochemical behavior in solution. Conversely, when mechanical force was applied to *m*DPAC, mechanical constraints inhibited photo-planarization, resulting in a configuration controlled solely by mechanical inputs.

3. CONCLUSION

In this study, we introduced and characterized a novel mechanoresponsive molecular gear, *m*DPAC, and successfully incorporated it into hydrogels to explore its dynamic mechanochromic properties. The mechanoresponsive mechanism of *m*DPAC hinged on the simultaneous change in its bending and bay angles. Mechanical stretching enlarged *m*DPAC's bay angle, which in turn led to an increase in bending angle. These configurational changes in the phenazine moiety extended its conjugation length, leading to a pronounced red shift in fluorescence. Such a mechanically induced fluorescence change establishes *m*DPAC as a unique mechanophore, showcasing its dynamic mechanosensitivity and multicolored mechanochromism.

Unlike conventional mechanophores, which demand mechanical force along the axis or in alignment with mechanosensitive bonds, *m*DPAC features a unique orientation of the applied force perpendicular to the bending angle of the phenazine plane. This distinct feature emerges from the worm gear-like interconnection between *m*DPAC's bending and bay angles. Our experimental emission data, supported by extensive DFT and MD simulations, have unraveled the complex mechanism underlying *m*DPAC's mechanochemical response. These findings affirm *m*DPAC's mechanochemical reactivity and underscore the critical role of steric hindrance between hydrogen atoms from different *m*DPAC moieties in modulating its molecular gearing and mechanoresponsive activity. Moreover, *m*DPAC's great compatibility with hydrogels underlines its potential for biological applications in aqueous environments. It is feasible for biological systems and hydrogel-based materials as a dynamic molecular force sensor and mapping tool. *m*DPAC's multicolored mechanochromism further enables real-time force sensing, allowing for visual force detection and precise force quantification.

References

1. (a) Liepuoniute, I.; Jellen, M. J.; Garcia-Garibay, M. A. Correlated motion and mechanical gearing in amphidynamic crystalline molecular machines. *Chem. Sci.* **2020,** *11* (48), 12994-13007. DOI: 10.1039/D0SC04495D; (b) Singhania, A.; Kalita, S.; Chettri, P.; Ghosh, S. Accounts of applied molecular rotors and rotary motors: recent advances. *Nanoscale Adv.* **2023,** *5* (12), 3177-3208. DOI: 10.1039/D3NA00010A; (c) Kay, E. R.; Leigh, D. A.; Zerbetto, F. Synthetic Molecular Motors and Mechanical Machines. *Angew. Chem. Int. Ed.* **2007,** *46* (1-2), 72-191. DOI: 10.1002/anie.200504313
2. (a) Gisbert, Y.; Abid, S.; Kammerer, C.; Rapenne, G. Molecular Gears: From Solution to Surfaces. *Chem. Eur. J.* **2021,** *27* (47), 12019-12031. DOI: 10.1002/chem.202101489; (b) Kottas, G. S.; Clarke, L. I.; Horinek, D.; Michl, J. Artificial Molecular Rotors. *Chem. Rev.* **2005,** *105* (4), 1281-1376. DOI: 10.1021/cr0300993
3. (a) Huang, F.; Wang, G.; Ma, L.; Wang, Y.; Chen, X.; Che, Y.; Jiang, H. Molecular Spur Gears Based on a Switchable Quinquepyridine Foldamer Acting as a Stator. *J. Org. Chem.* **2017,** *82* (23), 12106-12111. DOI: 10.1021/acs.joc.7b01864; (b) Jiang, X.; Yang, S.; Jellen, M. J.; Houk, K. N.; Garcia-Garibay, M. Molecular Spur Gears with Triptycene Rotators and a Norbornane-Based Stator. *Org. Lett.* **2020,** *22* (11), 4049-4052. DOI: 10.1021/acs.orglett.0c01029; (c) Bryan, J. C.; Sachleben, R. A.; Gakh, A. A.; Bunick, G. J. *J. Chem. Crystallogr.* **1999,** *29* (5), 513-521. DOI: 10.1023/a:1009535632237
4. (a) Sanada, K.; Ube, H.; Shionoya, M. Rotational Control of a Dirhodium-Centered Supramolecular Four-Gear System by Ligand Exchange. *J. Am. Chem. Soc.* **2016,** *138* (9), 2945-2948. DOI: 10.1021/jacs.5b13515; (b) Nakamura, M.; Kishimoto, K.; Kobori, Y.; Abe, T.; Yoza, K.; Kobayashi, K. Self-Assembled Molecular Gear: A 4:1 Complex of Rh(III)Cl Tetraarylporphyrin and Tetra(p-pyridyl)cavitand. *J. Am. Chem. Soc.* **2016,** *138* (38), 12564-12577. DOI: 10.1021/jacs.6b07284; (c) Toyota, S.; Kawahata, K.; Sugahara, K.; Wakamatsu, K.; Iwanaga, T. Triple and Quadruple Triptycene Gears in Rigid Macrocyclic Frameworks. *Eur. J. Org. Chem.* **2017,** *2017* (37), 5696-5707. DOI: 10.1002/ejoc.201701067
5. (a) Ube, H.; Yasuda, Y.; Sato, H.; Shionoya, M. Metal-centred azaphosphatriptycene gear with a photo- and thermally driven mechanical switching function based on coordination isomerism. *Nat. Commun.* **2017,** *8* (1), 14296. DOI: 10.1038/ncomms14296; (b) Shirai, Y.; Osgood, A. J.; Zhao, Y.; Kelly, K. F.; Tour, J. M. Directional Control in Thermally Driven Single-Molecule Nanocars. *Nano Lett.* **2005,** *5* (11), 2330-2334. DOI: 10.1021/nl051915k
6. (a) Koumura, N.; Zijlstra, R. W. J.; Van Delden, R. A.; Harada, N.; Feringa, B. L. Light-driven monodirectional molecular rotor. *Nature* **1999,** *401* (6749), 152-155. DOI: 10.1038/43646; (b)

Foy, J. T.; Li, Q.; Goujon, A.; Colard-Itté, J.-R.; Fuks, G.; Moulin, E.; Schiffmann, O.; Dattler, D.; Funeriu, D. P.; Giuseppone, N. Dual-light control of nanomachines that integrate motor and modulator subunits. *Nat. Nanotechnol.* **2017,** *12* (6), 540-545. DOI: 10.1038/nnano.2017.28; (c) Gerwien, A.; Gnannt, F.; Mayer, P.; Dube, H. Photogearing as a concept for translation of precise motions at the nanoscale. *Nat. Chem.* **2022,** *14* (6), 670-676. DOI: 10.1038/s41557-022-00917-0

7. Lin, H. H.; Croy, A.; Gutierrez, R.; Joachim, C.; Cuniberti, G. Current-induced rotations of molecular gears. *J. Phys. Commun.* **2019,** *3* (2), 025011. DOI: 10.1088/2399-6528/ab0731
8. (a) Ube, H.; Yamada, R.; Ishida, J.-i.; Sato, H.; Shiro, M.; Shionoya, M. A Circularly Arranged Sextuple Triptycene Gear Molecule. *J. Am. Chem. Soc.* **2017,** *139* (46), 16470-16473. DOI: 10.1021/jacs.7b09439; (b) Ogi, S.; Ikeda, T.; Wakabayashi, R.; Shinkai, S.; Takeuchi, M. Mechanically Interlocked Porphyrin Gears Propagating Two Different Rotational Frequencies. *Eur. J. Org. Chem.* **2011,** *2011* (10), 1831-1836. DOI: 10.1002/ejoc.201001656; (c) Goswami, A.; Saha, S.; Biswas, P. K.; Schmittel, M. (Nano)mechanical Motion Triggered by Metal Coordination: from Functional Devices to Networked Multicomponent Catalytic Machinery. *Chem. Rev.* **2020,** *120* (1), 125-199. DOI: 10.1021/acs.chemrev.9b00159; (d) Baroncini, M.; Silvi, S.; Credi, A. Photo- and Redox-Driven Artificial Molecular Motors. *Chem. Rev.* **2020,** *120* (1), 200-268. DOI: 10.1021/acs.chemrev.9b00291
9. (a) Ghanem, M. A.; Basu, A.; Behrou, R.; Boechler, N.; Boydston, A. J.; Craig, S. L.; Lin, Y.; Lynde, B. E.; Nelson, A.; Shen, H.; Storti, D. W. The role of polymer mechanochemistry in responsive materials and additive manufacturing. *Nat. Rev. Mater.* **2021,** *6* (1), 84-98. DOI: 10.1038/s41578-020-00249-w; (b) Klok, H.-A.; Herrmann, A.; Göstl, R. Force ahead: Emerging Applications and Opportunities of Polymer Mechanochemistry. *ACS Polym. Au* **2022,** *2* (4), 208-212. DOI: 10.1021/acspolymersau.2c00029
10. (a) Wang, N. Review of cellular mechanotransduction. *J. Phys. D: Appl. Phys.* **2017,** *50* (23), 233002. DOI: 10.1088/1361-6463/aa6e18; (b) De Belly, H.; Paluch, E. K.; Chalut, K. J. Interplay between mechanics and signalling in regulating cell fate. *Nat. Rev. Mol. Cell Biol.* **2022,** *23* (7), 465-480. DOI: 10.1038/s41580-022-00472-z
11. (a) Kassem, S.; van Leeuwen, T.; Lubbe, A. S.; Wilson, M. R.; Feringa, B. L.; Leigh, D. A. Artificial molecular motors. *Chem. Soc. Rev.* **2017,** *46* (9), 2592-2621. DOI: 10.1039/C7CS00245A; (b) García-López, V.; Liu, D.; Tour, J. M. Light-Activated Organic Molecular Motors and Their Applications. *Chem. Rev.* **2020,** *120* (1), 79-124. DOI: 10.1021/acs.chemrev.9b00221; (c) Dattler, D.; Fuks, G.; Heiser, J.; Moulin, E.; Perrot, A.; Yao, X.; Giuseppone, N. Design of Collective Motions from Synthetic Molecular Switches, Rotors, and Motors. *Chem. Rev.* **2020,** *120* (1), 310-433. DOI: 10.1021/acs.chemrev.9b00288

12. (a) Manzano, C.; Soe, W. H.; Wong, H. S.; Ample, F.; Gourdon, A.; Chandrasekhar, N.; Joachim, C. Step-by-step rotation of a molecule-gear mounted on an atomic-scale axis. *Nat. Mater.* **2009,** *8* (7), 576-579. DOI: 10.1038/nmat2467; (b) Zhang, Y.; Kersell, H.; Stefak, R.; Echeverria, J.; Iancu, V.; Perera, U. G. E.; Li, Y.; Deshpande, A.; Braun, K. F.; Joachim, C.; Rapenne, G.; Hla, S. W. Simultaneous and coordinated rotational switching of all molecular rotors in a network. *Nat. Nanotechnol.* **2016,** *11* (8), 706-712. DOI: 10.1038/nnano.2016.69; (c) Kudernac, T.; Ruangsupapichat, N.; Parschau, M.; Maciá, B.; Katsonis, N.; Harutyunyan, S. R.; Ernst, K.-H.; Feringa, B. L. Electrically driven directional motion of a four-wheeled molecule on a metal surface. *Nature* **2011,** *479* (7372), 208-211. DOI: 10.1038/nature10587; (d) Tierney, H. L.; Murphy, C. J.; Jewell, A. D.; Baber, A. E.; Iski, E. V.; Khodaverdian, H. Y.; McGuire, A. F.; Klebanov, N.; Sykes, E. C. H. Experimental demonstration of a single-molecule electric motor. *Nat. Nanotechnol.* **2011,** *6* (10), 625-629. DOI: 10.1038/nnano.2011.142
13. (a) Zhang, Z.; Sun, G.; Chen, W.; Su, J.; Tian, H. The endeavor of vibration-induced emission (VIE) for dynamic emissions. *Chem. Sci.* **2020,** *11* (29), 7525-7537. DOI: 10.1039/d0sc01591a; (b) Zhang, Z.; Jin, X.; Sun, X.; Su, J.; Qu, D.-H. Vibration-induced emission: Dynamic multiple intrinsic luminescence. *Coord. Chem. Rev.* **2022,** *472*, 214768. DOI: 10.1016/j.ccr.2022.214768
14. (a) Zhang, J. L.; Zhong, J. Q.; Lin, J. D.; Hu, W. P.; Wu, K.; Xu, G. Q.; Wee, A. T. S.; Chen, W. Towards single molecule switches. *Chem. Soc. Rev.* **2015,** *44* (10), 2998-3022. DOI: 10.1039/c4cs00377b; (b) Fitzmaurice, O.; Bartkowski, M.; Giordani, S. Molecular Switches—Tools for Imparting Control in Drug Delivery Systems. *Front. Chem.* **2022,** *10*, 859450. DOI: 10.3389/fchem.2022.859450; (c) Wang, G.; Zhang, J. Photoresponsive molecular switches for biotechnology. *J. Photochem. Photobiol. C* **2012,** *13* (4), 299-309. DOI: 10.1016/j.jphotochemrev.2012.06.002
15. (a) Zhang, Z.; Song, W.; Su, J.; Tian, H. Vibration‐Induced Emission (VIE) of *N,N′*-Disubstituted‐Dihydribenzo[*a,c*]phenazines: Fundamental Understanding and Emerging Applications. *Adv. Funct. Mater.* **2020,** *30* (2), 1902803. DOI: 10.1002/adfm.201902803; (b) Wang, N.; Xin, C.; Li, Z.; Zhang, G.; Bai, L.; Gong, Q.; Xu, C.; Han, X.; Yu, C.; Li, L.; Huang, W. A reversible fluorescent probe for directly monitoring protein-small molecules interaction utilizing vibration-induced emission. *Dyes Pigm.* **2019,** *163*, 425-432. DOI: 10.1016/j.dyepig.2018.12.027
16. (a) Zhang, Z.; Wu, Y.-S.; Tang, K.-C.; Chen, C.-L.; Ho, J.-W.; Su, J.; Tian, H.; Chou, P.-T. Excited-State Conformational/Electronic Responses of Saddle-Shaped N,N′-Disubstituted-Dihydrodibenzo[a,c]phenazines: Wide-Tuning Emission from Red to Deep Blue and White Light Combination. *J. Am. Chem. Soc.* **2015,** *137* (26), 8509-8520. DOI: 10.1021/jacs.5b03491; (b)

Chen, W.; Chen, C.-L.; Zhang, Z.; Chen, Y.-A.; Chao, W.-C.; Su, J.; Tian, H.; Chou, P.-T. Snapshotting the Excited-State Planarization of Chemically Locked N,N′ -Disubstituted Dihydrodibenzo[a,c]phenazines. *J. Am. Chem. Soc.* **2017,** *139* (4), 1636-1644. DOI: 10.1021/jacs.6b11789; (c) Zhang, Z.; Chen, C.-L.; Chen, Y.-A.; Wei, Y.-C.; Su, J.; Tian, H.; Chou, P.-T. Tuning the Conformation and Color of Conjugated Polyheterocyclic Skeletons by Installing ortho-Methyl Groups. *Angew. Chem. Int. Ed.* **2018,** *57* (31), 9880-9884. DOI: 10.1002/anie.201806385

17. (a) Beyer, M. K.; Clausen-Schaumann, H. Mechanochemistry: The Mechanical Activation of Covalent Bonds. *Chem. Rev.* **2005,** *105* (8), 2921-2948. DOI: 10.1021/cr030697h; (b) Willis-Fox, N.; Rognin, E.; Aljohani, T. A.; Daly, R. Polymer Mechanochemistry: Manufacturing Is Now a Force to Be Reckoned With. *Chem* **2018,** *4* (11), 2499-2537. DOI: 10.1016/j.chempr.2018.08.001
18. (a) Hickenboth, C. R.; Moore, J. S.; White, S. R.; Sottos, N. R.; Baudry, J.; Wilson, S. R. Biasing reaction pathways with mechanical force. *Nature* **2007,** *446* (7134), 423-427. DOI: 10.1038/nature05681; (b) Wang, J.; Kouznetsova, T. B.; Niu, Z.; Ong, M. T.; Klukovich, H. M.; Rheingold, A. L.; Martinez, T. J.; Craig, S. L. Inducing and quantifying forbidden reactivity with single-molecule polymer mechanochemistry. *Nat. Chem.* **2015,** *7* (4), 323-327. DOI: 10.1038/nchem.2185
19. (a) Wang, Z.; Zheng, X.; Ouchi, T.; Kouznetsova, T. B.; Beech, H. K.; Av-Ron, S.; Matsuda, T.; Bowser, B. H.; Wang, S.; Johnson, J. A.; Kalow, J. A.; Olsen, B. D.; Gong, J. P.; Rubinstein, M.; Craig, S. L. Toughening hydrogels through force-triggered chemical reactions that lengthen polymer strands. *Science* **2021,** *374* (6564), 193-196. DOI: 10.1126/science.abg2689; (b) Chen, Y.; Mellot, G.; Van Luijk, D.; Creton, C.; Sijbesma, R. P. Mechanochemical tools for polymer materials. *Chem. Soc. Rev.* **2021,** *50* (6), 4100-4140. DOI: 10.1039/d0cs00940g
20. (a) Chen, X.-X.; Bayard, F.; Gonzalez-Sanchis, N.; Pamungkas, K. K. P.; Sakai, N.; Matile, S. Fluorescent Flippers: Small-Molecule Probes to Image Membrane Tension in Living Systems. *Angew. Chem. Int. Ed.* **2023,** *62* (20), e202217868. DOI: 10.1002/anie.202217868; (b) Yao, Y.; McFadden, M. E.; Luo, S. M.; Barber, R. W.; Kang, E.; Bar-Zion, A.; Smith, C. A. B.; Jin, Z.; Legendre, M.; Ling, B.; Malounda, D.; Torres, A.; Hamza, T.; Edwards, C. E. R.; Shapiro, M. G.; Robb, M. J. Remote control of mechanochemical reactions under physiological conditions using biocompatible focused ultrasound. *Proc. Natl. Acad. Sci.* **2023,** *120* (39), e2309822120. DOI: 10.1073/pnas.2309822120; (c) Huang, W.; Wu, X.; Gao, X.; Yu, Y.; Lei, H.; Zhu, Z.; Shi, Y.; Chen, Y.; Qin, M.; Wang, W.; Cao, Y. Maleimide-thiol adducts stabilized through stretching. *Nat. Chem.* **2019,** *11* (4), 310-319. DOI: 10.1038/s41557-018-0209-2; (d) Xuan, M.; Fan, J.; Khiêm, V. N.; Zou, M.; Brenske, K. O.; Mourran, A.; Vinokur, R.; Zheng, L.; Itskov, M.; Göstl, R.;

Herrmann, A. Polymer Mechanochemistry in Microbubbles. *Adv. Mater.* **2023,** *35* (47), 2305130. DOI: 10.1002/adma.202305130

21. (a) Li, J.; Nagamani, C.; Moore, J. S. Polymer Mechanochemistry: From Destructive to Productive. *Acc. Chem. Res.* **2015,** *48* (8), 2181-2190. DOI: 10.1021/acs.accounts.5b00184; (b) Lloyd, E. M.; Vakil, J. R.; Yao, Y.; Sottos, N. R.; Craig, S. L. Covalent Mechanochemistry and Contemporary Polymer Network Chemistry: A Marriage in the Making. *J. Am. Chem. Soc.* **2023,** *145* (2), 751-768. DOI: 10.1021/jacs.2c09623
22. Davis, D. A.; Hamilton, A.; Yang, J.; Cremar, L. D.; Van Gough, D.; Potisek, S. L.; Ong, M. T.; Braun, P. V.; Martinez, T. J.; White, S. R.; Moore, J. S.; Sottos, N. R. Force-Induced Activation of Covalent Bonds in Mechanoresponsive Polymeric Materials. *Nature* **2009,** *459* (7243), 68-72. DOI: 10.1038/nature07970
23. Robb, M. J.; Kim, T. A.; Halmes, A. J.; White, S. R.; Sottos, N. R.; Moore, J. S. Regioisomer-Specific Mechanochromism of Naphthopyran in Polymeric Materials. *J. Am. Chem. Soc.* **2016,** *138* (38), 12328-12331. DOI: 10.1021/jacs.6b07610
24. Sumi, T.; Goseki, R.; Otsuka, H. Tetraarylsuccinonitriles as mechanochromophores to generate highly stable luminescent carbon-centered radicals. *Chem. Commun.* **2017,** *53* (87), 11885-11888. DOI: 10.1039/c7cc06913h
25. Yamakado, T.; Saito, S. Ratiometric Flapping Force Probe That Works in Polymer Gels. *J. Am. Chem. Soc.* **2022,** *144* (6), 2804-2815. DOI: 10.1021/jacs.1c12955
26. Hertel, R.; Maftuhin, W.; Walter, M.; Sommer, M. Conformer Ring Flip Enhances Mechanochromic Performance of *ansa*-Donor–Acceptor–Donor Mechanochromic Torsional Springs. *J. Am. Chem. Soc.* **2022,** *144* (48), 21897-21907. DOI: 10.1021/jacs.2c06712
27. Zhang, C.; Fu, X.; Hu, X. Harnessing the Conformer/Atropisomer-Dependent Photochromism of Diarylethene Photoswitches and Forcing a Diarylethene Atropisomer to Its Configurational Diastereomers with Polymer Mechanochemistry. *Synlett* **2023**, Article ASAP. DOI: 10.1055/s-0042-1751536. DOI: 10.1055/s-0042-1751536
28. Li, Y.; Xue, B.; Yang, J.; Jiang, J.; Liu, J.; Zhou, Y.; Zhang, J.; Wu, M.; Yuan, Y.; Zhu, Z.; Wang, Z. J.; Chen, Y.; Harabuchi, Y.; Nakajima, T.; Wang, W.; Maeda, S.; Gong, J. P.; Cao, Y. Azobenzene as a photoswitchable mechanophore. *Nat. Chem.* **2023**, Article ASAP. DOI: 10.1038/s41557-023-01389-6. DOI: 10.1038/s41557-023-01389-6
29. Jin, X.; Guo, S.; Wang, X.; Cong, M.; Chen, J.; Zhang, Z.; Su, J.; Qu, D.-H.; Tian, H. Sequential Multistep Excited-State Structural Transformations in N,N′ -Diphenyl-dihydrodibenzo[a,c]phenazine Fluorophores. *Angew. Chem. Int. Ed.* **2023,** *62* (29), e202305572. DOI: 10.1002/anie.202305572

30. (a) Watabe, T.; Otsuka, H. Swelling-induced Mechanochromism in Multinetwork Polymers. *Angew. Chem. Int. Ed.* **2023,** *62* (9), e202216469. DOI: 10.1002/anie.202216469; (b) Metze, F. K.; Sant, S.; Meng, Z.; Klok, H.-A.; Kaur, K. Swelling-Activated, Soft Mechanochemistry in Polymer Materials. *Langmuir* **2023,** *39* (10), 3546-3557. DOI: 10.1021/acs.langmuir.2c02801; (c) Lee, C. K.; Diesendruck, C. E.; Lu, E.; Pickett, A. N.; May, P. A.; Moore, J. S.; Braun, P. V. Solvent Swelling Activation of a Mechanophore in a Polymer Network. *Macromolecules* **2014,** *47* (8), 2690-2694. DOI: 10.1021/ma500195h
31. Beyer, M. K. The mechanical strength of a covalent bond calculated by density functional theory. *J. Chem. Phys.* **2000,** *112* (17), 7307-7312. DOI: 10.1063/1.481330
32. Klein, I. M.; Husic, C. C.; Kovács, D. P.; Choquette, N. J.; Robb, M. J. Validation of the CoGEF Method as a Predictive Tool for Polymer Mechanochemistry. *J. Am. Chem. Soc.* **2020,** *142* (38), 16364-16381. DOI: 10.1021/jacs.0c06868
33. Lu, T. Simple, reliable, and universal metrics of molecular planarity. *J. Mol. Model.* **2021,** *27* (9). DOI: 10.1007/s00894-021-04884-0
34. Lu, T.; Chen, F. Multiwfn: A multifunctional wavefunction analyzer. *J. Comput. Chem.* **2012,** *33* (5), 580-592. DOI: 10.1002/jcc.22885
35. (a) Tsirelson, V.; Stash, A. Analyzing experimental electron density with the localized-orbital locator. *Acta Crystallogr. Sect. B* **2002,** *58* (5), 780-785. DOI: 10.1107/S0108768102012338; (b) Schmider, H. L.; Becke, A. D. Chemical content of the kinetic energy density. *J. Mol. Struct.* **2000,** *527* (1), 51-61. DOI: 10.1016/S0166-1280(00)00477-2
36. Liu, Z.; Lu, T.; Hua, S.; Yu, Y. Aromaticity of Hückel and Möbius Topologies Involved in Conformation Conversion of Macrocyclic [32]Octaphyrin(1.0.1.0.1.0.1.0): Refined Evidence from Multiple Visual Criteria. *J. Phys. Chem. C* **2019,** *123* (30), 18593-18599. DOI: 10.1021/acs.jpcc.9b06302
37. Lu, T.; Chen, Q. A simple method of identifying π orbitals for non-planar systems and a protocol of studying π electronic structure. *Theor. Chem. Acc.* **2020,** *139* (2). DOI: 10.1007/s00214-019-2541-z
38. Humphrey, W.; Dalke, A.; Schulten, K. VMD: Visual molecular dynamics. *Journal of Molecular Graphics* **1996,** *14* (1), 33-38. DOI: 10.1016/0263-7855(96)00018-5
39. Adamo, C.; Barone, V. Toward reliable density functional methods without adjustable parameters: The PBE0 model. *J. Chem. Phys.* **1999,** *110* (13), 6158-6170. DOI: 10.1063/1.478522
40. (a) Tomasi, J.; Mennucci, B.; Cammi, R. Quantum Mechanical Continuum Solvation Models. *Chem. Rev.* **2005,** *105* (8), 2999-3094. DOI: 10.1021/cr9904009; (b) Miertuš, S.; Scrocco, E.; Tomasi, J. Electrostatic interaction of a solute with a continuum. A direct utilizaion of AB initio

molecular potentials for the prevision of solvent effects. *Chem. Phys.* **1981,** *55* (1), 117-129. DOI: 10.1016/0301-0104(81)85090-2; (c) Miertuš, S.; Tomasi, J. Approximate evaluations of the electrostatic free energy and internal energy changes in solution processes. *Chem. Phys.* **1982,** *65* (2), 239-245. DOI: 10.1016/0301-0104(82)85072-6; (d) Pascual-ahuir, J. L.; Silla, E.; Tuñon, I. GEPOL: An improved description of molecular surfaces. III. A new algorithm for the computation of a solvent-excluding surface. *J. Comput. Chem.* **1994,** *15* (10), 1127-1138. DOI: 10.1002/jcc.540151009

41. (a) Grimme, S.; Bannwarth, C.; Shushkov, P. A Robust and Accurate Tight-Binding Quantum Chemical Method for Structures, Vibrational Frequencies, and Noncovalent Interactions of Large Molecular Systems Parametrized for All spd-Block Elements (Z = 1–86). *J. Chem. Theory Comput.* **2017,** *13* (5), 1989-2009. DOI: 10.1021/acs.jctc.7b00118; (b) Bannwarth, C.; Caldeweyher, E.; Ehlert, S.; Hansen, A.; Pracht, P.; Seibert, J.; Spicher, S.; Grimme, S. Extended tight-binding quantum chemistry methods. *Wiley Interdiscip. Rev. Comput. Mol. Sci.* **2021,** *11* (2), e1493. DOI: 10.1002/wcms.1493; (c) Bannwarth, C.; Ehlert, S.; Grimme, S. GFN2-xTB—An Accurate and Broadly Parametrized Self-Consistent Tight-Binding Quantum Chemical Method with Multipole Electrostatics and Density-Dependent Dispersion Contributions. *J. Chem. Theory Comput.* **2019,** *15* (3), 1652-1671. DOI: 10.1021/acs.jctc.8b01176
42. (a) Kufareva, I.; Abagyan, R., Methods of Protein Structure Comparison. In *Homology Modeling: Methods and Protocols*, Humana Press: Totowa, NJ, 2012. DOI: 10.1007/978-1-61779-588-6_10; (b) Carugo, O. Statistical validation of the root-mean-square-distance, a measure of protein structural proximity. *Protein Eng. Des. Sel.* **2007,** *20* (1), 33-37. DOI: 10.1093/protein/gzl051; (c) Coutsias, E. A.; Seok, C.; Dill, K. A. Using quaternions to calculate RMSD. *J. Comput. Chem.* **2004,** *25* (15), 1849-1857. DOI: 10.1002/jcc.20110
43. Lu, T. *Molclus program, Version 1.12*. Beijing Kein Research Center for Natural Science: Beijing, China, **2018**. http://www.keinsci.com/research/molclus.html (accessed 2024-02-06)
44. Zhao, Y.; Truhlar, D. G. The M06 suite of density functionals for main group thermochemistry, thermochemical kinetics, noncovalent interactions, excited states, and transition elements: two new functionals and systematic testing of four M06-class functionals and 12 other function. *Theor. Chem. Acc.* **2008,** *120* (1-3), 215-241. DOI: 10.1007/s00214-007-0310-x
45. Stratmann, R. E.; Scuseria, G. E.; Frisch, M. J. An efficient implementation of time-dependent density-functional theory for the calculation of excitation energies of large molecules. *J. Chem. Phys.* **1998,** *109* (19), 8218-8224. DOI: 10.1063/1.477483